PROCEEDINGS OF SCIENCE

Machine learning driven reconstruction of cosmic-ray air showers for next generation radio arrays

The IceCube-Gen2 Collaboration

(a complete list of authors can be found at the end of the proceedings)

E-mail: paras.koundal@icecube.wisc.edu

Surface radio antenna-based measurements of cosmic-ray air showers present significant computational challenges in accurately reconstructing physics observables, in particular, the depth of shower maximum, X_{max}. State-of-the-art template fitting methods rely on extensive simulation libraries, limiting scalability. This work introduces a technique utilizing graph neural networks to reconstruct key air-shower parameters, in particular, direction and shower-core, energy, and X_{max}. For training and testing of the networks, we use a CoREAS simulation library made for a future enhancement of IceCube's surface array with radio antennas. The neural networks provide a scalable framework for large-scale data analysis for next-generation astroparticle observatories, such as IceCube-Gen2.

Corresponding authors: Paras Koundal[1]*,

[1] *Bartol Research Institute, Department of Physics and Astronomy, University of Delaware, U.S.A.*

* Presenter

39th International Cosmic Ray Conference (ICRC2025)
15–24 July 2025
Geneva, Switzerland

ICRC 2025
The Astroparticle Physics Conference
Geneva July 15-24, 2025

1. Introduction

Cosmic-ray (CR) primaries in atmosphere initiate a cascade of particles, generally referred to as an extensive air shower (EAS). The propagation of cascade particles (primarily e^+ and e^-) through Earth's atmosphere is responsible for radio emission. This emission can be measured in MHz frequency band using radio-antennas at detectors like the upcoming surface enhancement of IceCube Observatory [1, 2]. The radio footprint carries information about CR primary direction, energy, and primary type [3]. Radio-detection allows for almost a 100% duty cycle, and additionally, antennas are much cheaper to deploy than other kinds of cosmic-ray detectors. Because of significant improvements in understanding of radio-emission mechanisms, their measurement, and digital signal processing techniques, the method has gained prominence in the last two decades [4]. Radio-detection of EASs also allows an estimation of X_{max} , i.e., the atmospheric depth at which we expect the maxima in number of particles with lesser dependence on the choice of hadronic model. X_{max} is one of the most useful EAS observables to discriminate between the nuclei initiating the EASs [5].

Current radio-based observatories use surface detectors such as ice or water-based Cherenkov detectors and scintillators to provide the trigger for the radio antennas. The signal from the various EAS components at these surface detectors is then used to get an estimate of core-location, direction (zenith, azimuth), and energy. Radio detectors are then utilized to estimate X_{max} . Current state-of-the-art reconstruction methods rely on a template fitting approach by creating a library of simulation of simulations for each detected event (details upcoming in section 2). These methods hence have reliance on other detectors for some of the observables reconstruction, and are generally computationally expensive for X_{max} estimation. The computational-cost limits applicability to the CR observatories like the surface enhancement of IceCube, Pierre-Auger Observatory, SKA, and others. This work hence focuses on developing a pipeline utilizing both physics-motivated and Graph Neural Network (GNN) based reconstructions to provide a fast and computationally efficient solution, relying solely on measurements done using radio antennas. Section 2 provides a concise overview of the current state-of-the-art method, describes the simulations used for GNN training, mentions the applied quality cuts, and breakdowns the reconstruction pipeline shown in Figure 3. Section 3 presents the reconstruction performance for direction, core-location, energy, and X_{max} , followed up by the summary and outlook in Section 4.

2. Methodology

Current EAS reconstruction for radio detectors uses other detectors to estimate the core position, arrival direction, and energy, which are then used as seeds in simulations that vary only X_{max} . This allows for performing a χ^2-minimization analysis. This is done by antenna-wise comparison of the signal expectation at each location in the simulation with the observed signal. An aggregated χ^2 is obtained by combining all the χ^2 from antenna-wise comparison to get a single quantifier for each data-simulation pair [6]. This step is repeated for each of the simulations produced in the library for that particular data-event. The value corresponding to the minima in χ^2-values obtained by comparison of each data-simulation pair is then utilized to assign the estimated X_{max} for the specific event. The X_{max} resolution obtained from such methods is around 15-50 g·cm^{-2} [7]. It is evident that the currently used method not only relies on other detectors to provide an estimate of the core, direction, and energy, but also relies on the creation of a library of simulations for the estimation of $X_{\max}$ for each detected event. This creates dependencies and a computational bottleneck for any analysis.

The χ^2-method discussed earlier to estimate $X_{\max}$ is effectively a pattern matching method; we are trying to estimate which data-simulation pair looks most similar to each other. The central premise of this analysis is that the pattern-matching task inherent in the χ^2-analysis can be reformulated as a pattern recognition problem, which can be effectively addressed using deep neural networks (DNNs). Hence, instead of generating specific simulations for each data event to perform pattern matching, DNNs can be utilized by producing a library of simulations (covering the phase-space of all observable ranges) and training only once. This also allows fast estimates of various observables at inference time. Additionally, the pattern recognition task using DNNs can also be applied not only to estimate $X_{\max}$, but also to estimate the core, direction, and energy. Hence, utilizing DNNs not only prevents the computational bottleneck but also removes the reliance on other detectors for observable inference.

Using the proposed radio-antenna geometry of the planned IceCube-Gen2 Surface Array [8] as a case study, this work develops a reconstruction pipeline to estimate the location of the air shower core, the direction of arrival, the primary energy, and $X_{\max}$. The proposed array geometry is shown in Figure 1. For the purpose of this analysis, we use simulations produced using CoREAS [9], in the energy range $8.5 \leq \mathrm{Log}_{10}(\mathrm{Energy/GeV}) \leq 9.4$. The simulation library consists of an almost equal range of the different primary nuclei (p, He, O, and Fe), in a zenith range between 0-75 degrees. To increase statistics for training, each CoREAS simulation is resampled ten times and thrown at a random location within 2500 m from the center of the Surface Array (denoted as $\times$ in Figure 1). The antenna response is obtained by utilizing a star-pattern interpolation method, detailed in [10]. Each antenna has two perpendicular polarizations, which are simulated independently. For the majority of subsequent reconstructions, we utilize waveforms simulated at various antenna locations (and the corresponding polarizations). Modeled thermal and galactic noise (details in [10]) is also added to the waveforms. The analysis further applies a cut on signal-to-noise ratio (SNR) to be above 100 (motivated by results in [11]), and the minimum number of triggered antennas after SNR-cleaning should be at least 9. The remaining simulation set is then used for further analysis.

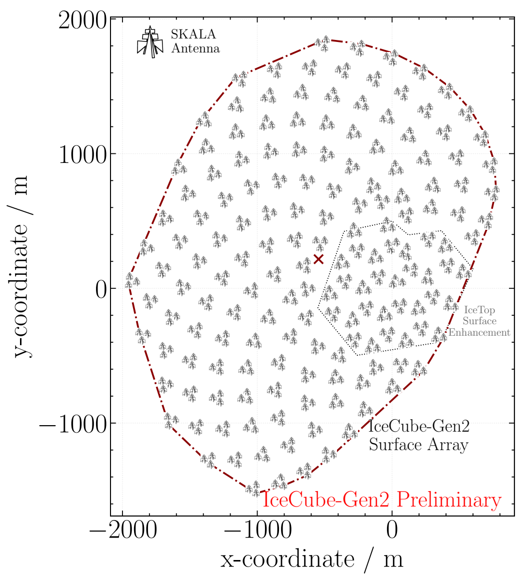

Figure 1: Proposed geometry of the Surface Array's radio component for IceCube-Gen2, featuring SKALA antennas. The dashed-dotted (-·-·-) red-line represents the boundary of the Surface Array, and red cross ($\times$) represents the geometric center of the array. The denser-array on top of IceTop is referred to as Surface Enhancement.

An artistic-expression of a radio waveform mentioned earlier is shown in Figure 2 (black curve). Each waveform can be reduced to a single representative value using the maximum instantaneous amplitude called as Hilbert Maximum (HM), which is derived from the Hilbert envelope. The Hilbert envelope provides the instantaneous amplitude of the waveform, allowing a concise characterization through its maximum value. In addition to the amplitude of the HM, we will also utilize the time corresponding to the HM. The time is measured with respect to the time measured at the antenna closest to the HM-amplitude weighted centroid of the triggered antennas. The HM-amplitude and HM-time will be used multiple times for the rest of the analysis. The pipeline used for the various reconstructions is presented in Figure 3. The pipeline utilizes both physics-based reconstructions and Graph Neural Network (GNN) based reconstructions. The multiple decisions made in the pipeline allow for fast and accurate reconstructions. The pipeline in multiple places uses GNNs, which are trained on graph-structured data. A graph is built of nodes and edges. For simplification, nodes can be interpreted as input pixels, and edges define the neighborhood between the nodes/pixels. The choice of GNNs over traditional CNNs was motivated by the irregular geometry of the proposed Surface Array, as well as the intention for this work to serve as a test case for other detector configurations with diverse geometries. Given their inherent flexibility and ability to operate on non-Euclidean domains, GNNs are the most natural architecture for this application. The following text will elaborate on each part of the pipeline.

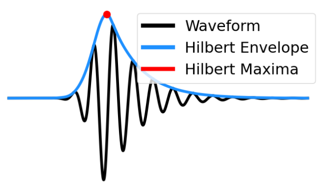

Figure 2: An example waveform with the Hilbert envelope and maxima marked.

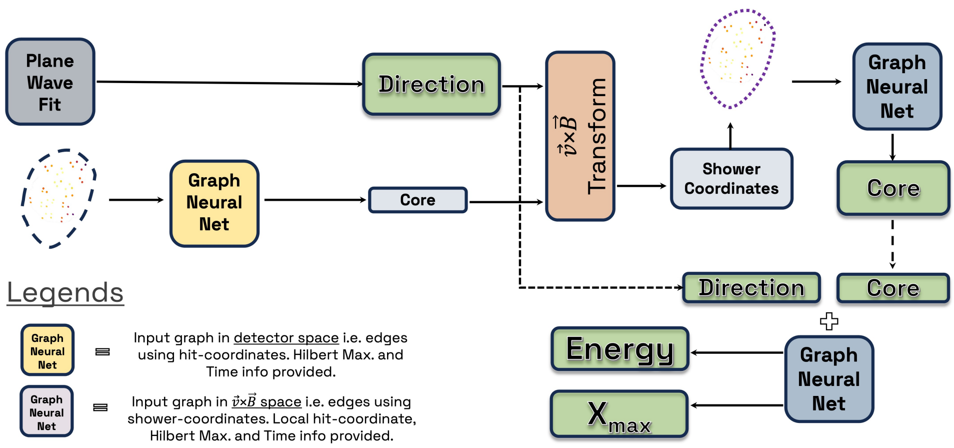

Figure 3: Schematic of the reconstruction pipeline combining physics-based and GNN-based methods. A plane-wave fit estimates the shower direction, while GNNs applied to detector-space and shower-coordinate graphs successively refine the core position. A final GNN predicts energy and $X_{\max}$. Read section 2 for details and section 3 for results.

2.1 Direction Reconstruction

To infer the arrival direction of the cosmic-ray primaries using an antenna array, we assume that the wavefront can be approximated as a plane wave. By fitting a plane wave to the arrival times (HM-time) of the radio pulses at multiple antenna positions, one can estimate the zenith and azimuth angles of the incoming radiation. Although improved methods are available, the plane-wave method has been tested in other radio arrays such as LOFAR [12, 13] and was able to obtain an angular resolution of about 1 degree. The plane-wave reconstruction first includes the evaluation of an estimated core location. This is done by computing an HM-amplitude weighted centroid over triggered antenna positions. To obtain the estimated direction, the method utilizes HM-time of a specific polarization at each antenna. A plane perpendicular to the shower-axis, centered at the estimated core, is considered, and the method then tries to fit the direction (zenith and azimuth) that best fits the expected time with the HM-time (i.e., measured time). The results obtained from plane-wave fit reconstruction for direction estimate will be discussed in subsection 3.1. Given that the current analysis remains at the proof-of-concept stage, this method is retained due to its simplicity and computational efficiency.

2.2 Core Reconstruction

Even though the core estimate obtained by plane-wave reconstruction discussed in subsection 2.1 is a good seed to perform direction reconstruction, the method by construction only allows for core reconstruction within the Surface-Array geometry, i.e., contained events. Furthermore, since we know that the lateral distribution of the radio signal on the ground is azimuthally asymmetric [14], a simple centroid estimation will be inherently biased. To provide a good core reconstruction, this work utilizes an iterative approach utilizing GNNs. The pipeline used for the core estimate using GNNs is shown in Figure 4. The architecture of the GNN used in Figure 4 (as well as the upcoming ones) is motivated by [15]. Only minor changes in hyperparameter choice (e.g., number of layers, number of hidden-nodes, normalization-layer choice, etc) have been done. The reconstruction is done in two steps. The first step (referred to as "Core Seed" in Figure 4) utilizes the triggered antennas to build a graph, i.e., antennas serve as nodes of the graph. Each node is connected to its 48 nearest neighbors, where the neighbors are evaluated by using the coordinate (x, y) of the antennas in the IceCube coordinate system. The amplitudes and times corresponding to HM for each polarization in an antenna waveform and the (x,y) coordinates of the antenna serve as features associated with each node. The network is trained to predict core location, with the true x and y coordinates from the simulation serving as the target variables. This is represented as "Core" in the "Core Seed" section of Figure 4. This step provides an improved core reconstruction (for both contained and un-contained EAS) than plane wave reconstruction.

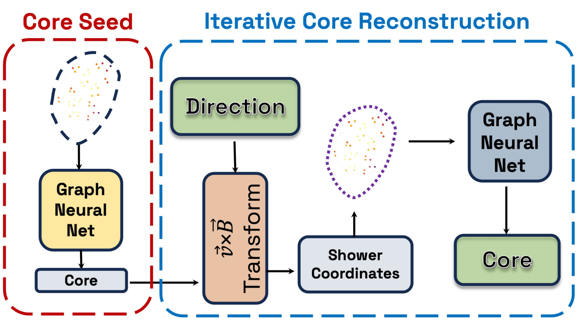

Figure 4: Part of pipeline from Figure 3 used for core estimate.

For vertical showers, the radio footprint in detector-coordinates generally looks circular. However, for more inclined showers the footprint of hits stretches out, and the footprint outline might appear as a thin ellipse [3]. Prior analysis experience from other observatories [6] has taught us that it is easier to reconstruct in shower-coordinates. $\vec{v} \times \vec{B}$ serves as the x-axis in this coordinate system, where $\vec{v}$ is the direction of the shower axis, and $\vec{B}$ is the direction of the geomagnetic field at the detector location. Naturally, $\vec{v} \times (\vec{v} \times \vec{B})$ serves as the second-axis, perpendicular to $\vec{v} \times \vec{B}$. Hence, the next step in the pipeline is to transform the detector-hits coordinates into shower-coordinates. The prior core-estimate from the GNN ("Core Seed") and the direction estimate from subsection 2.1 are used to perform this transformation and are represented as "$\vec{v} \times \vec{B}$ Transform" in Figure 3. The obtained coordinates are now utilized to build the edges of the graph in $\vec{v} \times \vec{B}$ (or shower-coordinate) space. Additionally, the shower-coordinates are used as additional features for each of the graph nodes. A new GNN is now trained again to predict the core location where the difference from the "Core Seed" step is in graph edge construction, and shower coordinates are an additional input at each node. The transform and the GNN prediction step are labeled as "Iterative Core Reconstruction" in Figure 4. Currently, this step is only performed once. However, it can be performed iteratively multiple times, with core prediction from each time serving as a seed for the $\vec{v} \times \vec{B}$ transform. The final core-reconstruction performance will be discussed in subsection 3.2.

2.3 Energy and X_{max} Reconstruction

Similar to the last step of core reconstruction, this step also trains a GNN where the graph is built in $\vec{v} \times \vec{B}$ space and the node features include detector-coordinates, shower-coordinates, HM amplitude, and time (for both polarizations). In addition to this, the reconstructed direction (from subsection 2.1) and core (from subsection 2.2) are also given as additional high-level inputs to the network. The network is trained to predict energy and distance to X_{max} . The distance to X_{max} is then used to calculate X_{max} . The combined prediction allows the network to also learn and resolve known degeneracies in footprint, which exist for different combinations of the two targets. The performance of energy and X_{max} reconstruction will be discussed in subsection 3.3.

3. Performance

The following text details the reconstruction accuracy of core position, arrival direction, energy, and X_{max} using the pipeline illustrated in Figure 3.

3.1 Direction

As discussed in subsection 2.1, plane-wave reconstruction is utilized to estimate the direction of the incident cosmic-ray primary. The reconstruction performance is shown as opening angle (Ψ) in Figure 5a. Opening angle is the angular separation between the predicted and true directions, defined by their respective zenith and azimuth angles for all and contained events. Contained events are a subset of all events defined as events whose true EAS core lies within the surface array footprint. The median opening angle between the reconstructed and true directions remains below 1 degree across the full energy range. For the subset, i.e., contained events, the reconstruction accuracy improves further, indicating enhanced angular resolution due to a larger fraction of radio-emission being detected at the antennas than otherwise. The worsening performance with increasing energy is likely due to of decreasing atmospheric depth between the observation level and X_{max} , consistent with expectations [16]. Reconstruction performance can potentially be improved by using improved estimates of the shape of the radio wavefront [14, 17] or GNN-based reconstructions (similar to the ones used in subsection 2.2 and subsection 2.3).

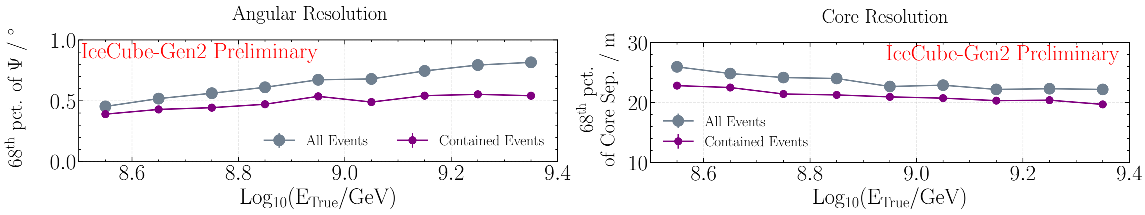

(a) Direction Reconstruction

(b) Core Reconstruction

Figure 5: Performance of direction (left) obtained using plane-wave reconstruction (Section 3.1) and core (right) reconstruction using an iterative Graph Neural Network (Section 3.2).

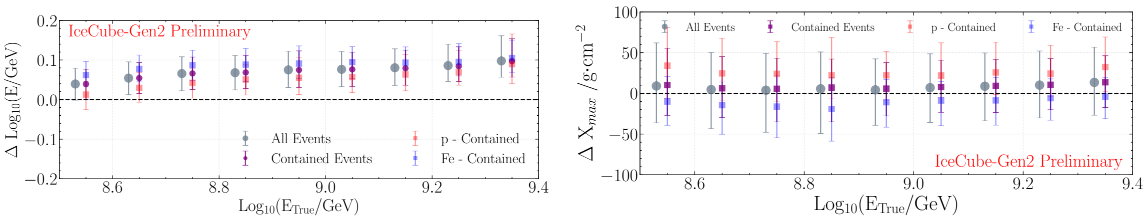

(a) Bias (median) and resolution (68% confidence interval) for energy prediction as a function of true energy.

(b) Bias and resolution for X_{max} prediction as a function of true energy.

Figure 6: Performance for energy (left) and X_{max} (right) reconstruction using Graph Neural Network. A shift in x-axis for "All Events" is introduced for easier visibility.

3.2 Core

As discussed in subsection 2.2, core reconstruction is performed using an iterative approach based on Graph Neural Networks (GNNs). The reconstruction performance, shown in Figure 5b, is quantified by the distance between the reconstructed and the true EAS core positions. The panel presents core resolution (68^{th} percentile of core separations) as a function of energy for all events as well as contained events. Contained events have better resolution across all energies, as expected. The core resolution remains relatively stable across the energy range, with a weak trend toward improved accuracy at higher energies. The work already presents the robustness of the GNN-based method for a variety of EAS geometries as well as its effectiveness in reconstructing both contained and uncontained events.

3.3 Energy and X_{max}

Similar to core prediction, energy and X_{max} reconstruction are also performed using GNNs. The reconstruction performance is shown in Figure 6, as a function of primary energy. The energy reconstruction shows a bias for all EASs as well as for contained. Ongoing work is trying to reduce this bias. The error bars (also for Figure 6b) indicate the 68 % confidence interval, and hence a measure of resolution. The figure also shows the energy bias and resolution for p and Fe. The bias and resolution performance for X_{max} prediction is shown in Figure 6b. The prediction shows small overall bias for all as well as contained EAS. Although it still has primary-type dependent bias. The resolution is of the order 50 g·cm^{-2}. Ongoing work is focusing on reducing the mass bias and improving the resolution.

4. Summary and Outlook

This work presents a pipeline that integrates physics-based reconstructions with Graph Neural Network reconstructions to reconstruct direction, core-location, energy, and $X_{\max}$, using only radio-antenna measurements. In the process, it reduces reliance on non-radio detectors and prevents the computational bottleneck of generating simulations for each detected event, as required by conventional reconstruction methods. Further improvement in energy and $X_{\max}$ reconstruction is needed. Overall, the work lays a foundation and demonstrate a new method to reconstruct both direction, core-location, energy, and $X_{\max}$ in a simulation-efficient manner. The pipeline can also be adapted to be used by hybrid observatories where reconstructions from other detectors can also be utilized or improved upon. A future development of this work also intends to test the reconstruction performance by adding measured noise and implementing denoising methods developed in [11].

References

[1] **IceCube** Collaboration, S. Shefali, *PoS, ICRC2025* (these proceedings) 394.

[2] **IceCube** Collaboration, M. Venugopal, *PoS, ICRC2025* (these proceedings) 427.

[3] F. G. Schröder, *Progress in Particle and Nuclear Physics* **93** (2017) 1–68.

[4] T. Huege, *Physics Reports* **620** (Mar., 2016) 1–52.

[5] B. Flaggs, A. Coleman, and F. G. Schröder, *Physical Review D* **109** no. 4, (Feb., 2024) .

[6] S. Buitink, A. Corstanje, J. E. Enriquez, *et al.*, *Phys. Rev. D* **90** (Oct, 2014) 082003.

[7] **Pierre Auger** Collaboration, *Physical Review Letters* **132** no. 2, (Jan., 2024) .

[8] **IceCube-Gen2** Collaboration, *Journal of Physics G: Nuclear and Particle Physics* **48** no. 6, (Apr., 2021) 060501.

[9] T. Huege, M. Ludwig, and C. W. James, *AIP Conference Proceedings* **1535** no. 1, (05, 2013) 128–132.

[10] **IceCube** Collaboration, *Journal of Instrumentation* **17** no. 06, (June, 2022) P06026.

[11] F. Schröder, A. Rehman, and I. Collaboration, "Application of Machine Learning to Identify Radio Pulses of Air Showers at the South Pole," ARENA2024. Nov., 2024.

[12] P. Schellart, A. Nelles, S. Buitink, A. Corstanje, *et al.*, *Astronomy amp; Astrophysics* **560** (Dec., 2013) A98.

[13] A. Corstanje, P. Schellart, A. Nelles, S. Buitink, *et al.*, *Astroparticle Physics* **61** (2015) 22–31.

[14] A. Coleman, "Model of the Lateral Distribution of the Radio Emission from Air Showers in the 70 - 350 MHz Frequency Band," ARENA2022. June, 2023.

[15] G. Li, M. Muller, A. Thabet, and B. Ghanem, "DeepGCNs: Can GCNs Go As Deep As CNNs?," pp. 9266–9275. IEEE, Oct., 2019. `https://github.com/pyg-team/pytorch_geometric/blob/master/examples/ogbn_proteins_deepgcn.py` (example).

[16] C. Glaser, M. Erdmann, J. R. Hörandel, T. Huege, and J. Schulz, *Journal of Cosmology and Astroparticle Physics* **2016** no. 09, (Sept., 2016) 024–024.

[17] W. Apel, J. Arteaga-Velázquez, *et al.*, *Journal of Cosmology and Astroparticle Physics* **2014** no. 09, (Sept., 2014) 025–025.

Full Author List: IceCube-Gen2 Collaboration

R. Abbasi[16], M. Ackermann[76], J. Adams[21], S. K. Agarwalla[46,a], J. A. Aguilar[10], M. Ahlers[25], J.M. Alameddine[26], S. Ali[39], N. M. Amin[52], K. Andeen[49], G. Anton[29], C. Argüelles[13], Y. Ashida[63], S. Athanasiadou[76], J. Audehm[1], S. N. Axani[52], R. Babu[27], X. Bai[60], A. Balagopal V.[52], M. Baricevic[46], S. W. Barwick[33], V. Basu[63], R. Bay[6], J. Becker Tjus[9,b], P. Behrens[1], J. Beise[74], C. Bellenghi[30], B. Benkel[76], S. BenZvi[62], D. Berley[22], E. Bernardini[58,c], D. Z. Besson[39], A. Bishop[46], E. Blaufuss[22], L. Bloom[70], S. Blot[76], M. Bohmer[30], F. Bontempo[34], J. Y. Book Motzkin[13], J. Borowka[1], C. Boscolo Meneguolo[58,c], S. Böser[47], O. Botner[74], J. Böttcher[1], S. Bouma[29], J. Braun[46], B. Brinson[4], Z. Brisson-Tsavoussis[36], R. T. Burley[2], M. Bustamante[25], D. Butterfield[46], M. A. Campana[59], K. Carloni[13], M. Cataldo[29], S. Chattopadhyay[46,a], N. Chau[10], Z. Chen[66], D. Chirkin[46], S. Choi[63], B. A. Clark[22], R. Clark[41], A. Coleman[74], P. Coleman[1], G. H. Collin[14], D. A. Coloma Borja[58], J. M. Conrad[14], R. Corley[63], D. F. Cowen[71,72], C. Deaconu[17,20], C. De Clercq[11], S. De Kockere[11], J. J. DeLaunay[71], D. Delgado[13], T. Delmeulle[10], S. Deng[1], A. Desai[46], P. Desiati[46], K. D. de Vries[11], G. de Wasseige[43], J. C. Díaz-Vélez[46], S. DiKerby[27], M. Dittmer[51], G. Do[1], A. Domi[29], L. Draper[63], L. Dueser[1], H. Dujmovic[46], D. Durnford[28], K. Dutta[47], M. A. DuVernois[46], T. Egby[5], T. Ehrhardt[47], L. Eidenschink[30], A. Eimer[29], P. Eller[30], E. Ellinger[75], D. Elsässer[26], R. Engel[34,35], H. Erpenbeck[46], W. Esmail[51], S. Eulig[13], J. Evans[22], J. J. Evans[48], P. A. Evenson[52], K. L. Fan[22], K. Fang[46], K. Farrag[15], A. R. Fazely[5], A. Fedynitch[68], N. Feigl[8], C. Finley[65], L. Fischer[76], B. Flaggs[52], D. Fox[71], A. Franckowiak[9], T. Fujii[56], S. Fukami[76], P. Fürst[1], J. Gallagher[45], E. Ganster[1], A. Garcia[13], G. Garg[46,a], E. Genton[13], L. Gerhardt[7], A. Ghadimi[70], P. Giri[40], C. Glaser[74], T. Glüsenkamp[74], S. Goswami[37,38], A. Granados[27], D. Grant[12], S. J. Gray[22], S. Griffin[46], S. Griswold[62], D. Guevel[46], C. Günther[1], P. Gutjahr[26], C. Ha[64], C. Haack[29], A. Hallgren[74], S. Hallmann[29,76], L. Halve[1], F. Halzen[46], L. Hamacher[1], M. Ha Minh[30], M. Handt[1], K. Hanson[46], J. Hardin[14], A. A. Harnisch[27], P. Hatch[36], A. Haungs[34], J. Häußler[1], D. Heinen[1], K. Helbing[75], J. Hellrung[9], B. Hendricks[72,73], B. Henke[27], L. Hennig[29], F. Henningsen[12], J. Henrichs[76], L. Heuermann[1], N. Heyer[74], S. Hickford[75], A. Hidvegi[65], C. Hill[15], G. C. Hill[2], K. D. Hoffman[22], B. Hoffmann[34], D. Hooper[46], S. Hori[46], K. Hoshina[46,d], M. Hostert[13], W. Hou[34], T. Huber[34], T. Huege[34], E. Huesca Santiago[76], K. Hultqvist[65], R. Hussain[46], K. Hymon[26,68], A. Ishihara[15], T. Ishii[56], W. Iwakiri[15], M. Jacquart[25,46], S. Jain[46], A. Jaitly[29,76], O. Janik[29], M. Jansson[43], M. Jeong[63], M. Jin[13], O. Kalekin[29], N. Kamp[13], D. Kang[34], W. Kang[59], X. Kang[59], A. Kappes[51], L. Kardum[26], T. Karg[76], M. Karl[30], A. Karle[46], A. Katil[28], T. Katori[41], U. Katz[29], M. Kauer[46], J. L. Kelley[46], M. Khanal[63], A. Khatee Zathul[46], A. Kheirandish[37,38], J. Kiryluk[66], M. Kleifges[34], C. Klein[29], S. R. Klein[6,7], T. Kobayashi[56], Y. Kobayashi[15], A. Kochocki[27], H. Kolanoski[8], T. Kontrimas[30], L. Köpke[47], C. Kopper[29], D. J. Koskinen[25], P. Koundal[52], M. Kowalski[8,76], T. Kozynets[25], I. Kravchenko[40], N. Krieger[9], J. Krishnamoorthi[46,a], T. Krishnan[13], E. Krupczak[27], A. Kumar[76], E. Kun[9], N. Kurahashi[59], N. Lad[76], L. Lallement Arnaud[10], M. J. Larson[22], F. Lauber[75], K. Leonard DeHolton[72], A. Leszczyńska[52], J. Liao[4], M. Liu[40], M. Liubarska[28], M. Lohan[50], J. LoSecco[55], C. Love[59], L. Lu[46], F. Lucarelli[31], Y. Lyu[6,7], J. Madsen[46], E. Magnus[11], K. B. M. Mahn[27], Y. Makino[46], E. Manao[30], S. Mancina[58,e], S. Mandalia[42], W. Marie Sainte[46], I. C. Mariş[10], S. Marka[54], Z. Marka[54], M. Marsee[70], L. Marten[1], I. Martinez-Soler[13], R. Maruyama[53], F. Mayhew[27], F. McNally[44], J. V. Mead[25], K. Meagher[46], S. Mechbal[76], A. Medina[24], M. Meier[15], Y. Merckx[11], L. Merten[9], Z. Meyers[76], M. Mikhailova[39], A. Millsop[41], J. Mitchell[5], T. Montaruli[31], R. W. Moore[28], Y. Morii[15], R. Morse[46], A. Mosbrugger[29], M. Moulai[46], D. Mousadi[29,76], T. Mukherjee[34], M. Muzio[71,72,73], R. Naab[76], M. Nakos[46], A. Narayan[50], U. Naumann[75], J. Necker[76], A. Nelles[29,76], L. Neste[65], M. Neumann[51], H. Niederhausen[27], M. U. Nisa[27], K. Noda[15], A. Noell[1], A. Novikov[52], E. Oberla[17,20], A. Obertacke Pollmann[15], V. O'Dell[46], A. Olivas[22], R. Orsoe[30], J. Osborn[46], E. O'Sullivan[74], V. Palusova[47], L. Papp[30], A. Parenti[10], N. Park[36], E. N. Paudel[70], L. Paul[60], C. Pérez de los Heros[74], T. Pernice[76], T. C. Petersen[25], J. Peterson[46], A. Pizzuto[46], M. Plum[60], A. Pontén[74], Y. Popovych[47], M. Prado Rodriguez[46], B. Pries[27], R. Procter-Murphy[22], G. T. Przybylski[7], L. Pyras[63], J. Rack-Helleis[47], N. Rad[76], M. Rameez[50], M. Ravn[74], K. Rawlins[3], Z. Rechav[46], A. Rehman[52], E. Resconi[30], S. Reusch[76], C. D. Rho[67], W. Rhode[26], B. Riedel[46], M. Riegel[34], A. Rifaie[75], E. J. Roberts[2], S. Robertson[6,7], M. Rongen[29], C. Rott[63], T. Ruhe[26], L. Ruohan[30], D. Ryckbosch[32], I. Safa[46], J. Saffer[35], D. Salazar-Gallegos[27], P. Sampathkumar[34], A. Sandrock[75], P. Sandstrom[46], G. Sanger-Johnson[27], M. Santander[70], S. Sarkar[57], J. Savelberg[1], P. Savina[46], P. Schaile[30], M. Schaufel[1], H. Schieler[34], S. Schindler[29], L. Schlickmann[47], B. Schlüter[51], F. Schlüter[10], N. Schmeisser[75], T. Schmidt[22], F. G. Schröder[34,52], L. Schumacher[29], S. Schwirn[1], S. Sclafani[22], D. Seckel[52], L. Seen[46], M. Seikh[39], Z. Selcuk[29,76], S. Seunarine[61], M. H. Shaevitz[54], R. Shah[59], S. Shefali[35], N. Shimizu[15], M. Silva[46], B. Skrzypek[6], R. Snihur[46], J. Soedingrekso[26], A. Søgaard[25], D. Soldin[63], P. Soldin[1], G. Sommani[9], C. Spannfellner[30], G. M. Spiczak[61], C. Spiering[76], J. Stachurska[32], M. Stamatikos[24], T. Stanev[52], T. Stezelberger[7], J. Stoffels[11], T. Stürwald[75], T. Stuttard[25], G. W. Sullivan[22], I. Taboada[4], A. Taketa[69], T. Tamang[50], H. K. M. Tanaka[69], S. Ter-Antonyan[5], A. Terliuk[30], M. Thiesmeyer[46], W. G. Thompson[13], J. Thwaites[46], S. Tilav[52], K. Tollefson[27], J. Torres[23,24], S. Toscano[10], D. Tosi[46], A. Trettin[76], Y. Tsunesada[56], J. P. Twagirayezu[27], A. K. Upadhyay[46,a], K. Upshaw[5], A. Vaidyanathan[49], N. Valtonen-Mattila[9,74], J. Valverde[49], J. Vandenbroucke[46], T. van Eeden[76], N. van Eijndhoven[11], L. van Rootselaar[26], J. van Santen[76], F. J. Vara Carbonell[51], F. Varsi[35], D. Veberic[34], J. Veitch-Michaelis[46], M. Venugopal[34], S. Vergara Carrasco[21], S. Verpoest[52], A. Vieregg[17,18,19,20], A. Vijai[22], J. Villarreal[14], C. Walck[65], A. Wang[4], D. Washington[72], C. Weaver[27], P. Weigel[14], A. Weindl[34], J. Weldert[47], A. Y. Wen[13], C. Wendt[46], J. Werthebach[26], M. Weyrauch[34], N. Whitehorn[27], C. H. Wiebusch[1], D. R. Williams[70], S. Wissel[71,72,73], L. Witthaus[26], M. Wolf[30], G. Wörner[34], G. Wrede[29], S. Wren[48], X. W. Xu[5], J. P. Yañez[28], Y. Yao[46], E. Yildizci[46], S. Yoshida[15], R. Young[39], F. Yu[13], S. Yu[63], T. Yuan[46], A. Zegarelli[9], S. Zhang[27], Z. Zhang[66], P. Zhelnin[13], S. Zierke[1], P. Zilberman[46], M. Zimmerman[46]

[1] III. Physikalisches Institut, RWTH Aachen University, D-52056 Aachen, Germany
[2] Department of Physics, University of Adelaide, Adelaide, 5005, Australia
[3] Dept. of Physics and Astronomy, University of Alaska Anchorage, 3211 Providence Dr., Anchorage, AK 99508, USA
[4] School of Physics and Center for Relativistic Astrophysics, Georgia Institute of Technology, Atlanta, GA 30332, USA
[5] Dept. of Physics, Southern University, Baton Rouge, LA 70813, USA

[6] Dept. of Physics, University of California, Berkeley, CA 94720, USA
[7] Lawrence Berkeley National Laboratory, Berkeley, CA 94720, USA
[8] Institut für Physik, Humboldt-Universität zu Berlin, D-12489 Berlin, Germany
[9] Fakultät für Physik & Astronomie, Ruhr-Universität Bochum, D-44780 Bochum, Germany
[10] Université Libre de Bruxelles, Science Faculty CP230, B-1050 Brussels, Belgium
[11] Vrije Universiteit Brussel (VUB), Dienst ELEM, B-1050 Brussels, Belgium
[12] Dept. of Physics, Simon Fraser University, Burnaby, BC V5A 1S6, Canada
[13] Department of Physics and Laboratory for Particle Physics and Cosmology, Harvard University, Cambridge, MA 02138, USA
[14] Dept. of Physics, Massachusetts Institute of Technology, Cambridge, MA 02139, USA
[15] Dept. of Physics and The International Center for Hadron Astrophysics, Chiba University, Chiba 263-8522, Japan
[16] Department of Physics, Loyola University Chicago, Chicago, IL 60660, USA
[17] Dept. of Astronomy and Astrophysics, University of Chicago, Chicago, IL 60637, USA
[18] Dept. of Physics, University of Chicago, Chicago, IL 60637, USA
[19] Enrico Fermi Institute, University of Chicago, Chicago, IL 60637, USA
[20] Kavli Institute for Cosmological Physics, University of Chicago, Chicago, IL 60637, USA
[21] Dept. of Physics and Astronomy, University of Canterbury, Private Bag 4800, Christchurch, New Zealand
[22] Dept. of Physics, University of Maryland, College Park, MD 20742, USA
[23] Dept. of Astronomy, Ohio State University, Columbus, OH 43210, USA
[24] Dept. of Physics and Center for Cosmology and Astro-Particle Physics, Ohio State University, Columbus, OH 43210, USA
[25] Niels Bohr Institute, University of Copenhagen, DK-2100 Copenhagen, Denmark
[26] Dept. of Physics, TU Dortmund University, D-44221 Dortmund, Germany
[27] Dept. of Physics and Astronomy, Michigan State University, East Lansing, MI 48824, USA
[28] Dept. of Physics, University of Alberta, Edmonton, Alberta, T6G 2E1, Canada
[29] Erlangen Centre for Astroparticle Physics, Friedrich-Alexander-Universität Erlangen-Nürnberg, D-91058 Erlangen, Germany
[30] Physik-department, Technische Universität München, D-85748 Garching, Germany
[31] Département de physique nucléaire et corpusculaire, Université de Genève, CH-1211 Genève, Switzerland
[32] Dept. of Physics and Astronomy, University of Gent, B-9000 Gent, Belgium
[33] Dept. of Physics and Astronomy, University of California, Irvine, CA 92697, USA
[34] Karlsruhe Institute of Technology, Institute for Astroparticle Physics, D-76021 Karlsruhe, Germany
[35] Karlsruhe Institute of Technology, Institute of Experimental Particle Physics, D-76021 Karlsruhe, Germany
[36] Dept. of Physics, Engineering Physics, and Astronomy, Queen's University, Kingston, ON K7L 3N6, Canada
[37] Department of Physics & Astronomy, University of Nevada, Las Vegas, NV 89154, USA
[38] Nevada Center for Astrophysics, University of Nevada, Las Vegas, NV 89154, USA
[39] Dept. of Physics and Astronomy, University of Kansas, Lawrence, KS 66045, USA
[40] Dept. of Physics and Astronomy, University of Nebraska–Lincoln, Lincoln, Nebraska 68588, USA
[41] Dept. of Physics, King's College London, London WC2R 2LS, United Kingdom
[42] School of Physics and Astronomy, Queen Mary University of London, London E1 4NS, United Kingdom
[43] Centre for Cosmology, Particle Physics and Phenomenology - CP3, Université catholique de Louvain, Louvain-la-Neuve, Belgium
[44] Department of Physics, Mercer University, Macon, GA 31207-0001, USA
[45] Dept. of Astronomy, University of Wisconsin—Madison, Madison, WI 53706, USA
[46] Dept. of Physics and Wisconsin IceCube Particle Astrophysics Center, University of Wisconsin—Madison, Madison, WI 53706, USA
[47] Institute of Physics, University of Mainz, Staudinger Weg 7, D-55099 Mainz, Germany
[48] School of Physics and Astronomy, The University of Manchester, Oxford Road, Manchester, M13 9PL, United Kingdom
[49] Department of Physics, Marquette University, Milwaukee, WI 53201, USA
[50] Dept. of High Energy Physics, Tata Institute of Fundamental Research, Colaba, Mumbai 400 005, India
[51] Institut für Kernphysik, Universität Münster, D-48149 Münster, Germany
[52] Bartol Research Institute and Dept. of Physics and Astronomy, University of Delaware, Newark, DE 19716, USA
[53] Dept. of Physics, Yale University, New Haven, CT 06520, USA
[54] Columbia Astrophysics and Nevis Laboratories, Columbia University, New York, NY 10027, USA
[55] Dept. of Physics, University of Notre Dame du Lac, 225 Nieuwland Science Hall, Notre Dame, IN 46556-5670, USA
[56] Graduate School of Science and NITEP, Osaka Metropolitan University, Osaka 558-8585, Japan
[57] Dept. of Physics, University of Oxford, Parks Road, Oxford OX1 3PU, United Kingdom
[58] Dipartimento di Fisica e Astronomia Galileo Galilei, Università Degli Studi di Padova, I-35122 Padova PD, Italy
[59] Dept. of Physics, Drexel University, 3141 Chestnut Street, Philadelphia, PA 19104, USA
[60] Physics Department, South Dakota School of Mines and Technology, Rapid City, SD 57701, USA
[61] Dept. of Physics, University of Wisconsin, River Falls, WI 54022, USA
[62] Dept. of Physics and Astronomy, University of Rochester, Rochester, NY 14627, USA
[63] Department of Physics and Astronomy, University of Utah, Salt Lake City, UT 84112, USA
[64] Dept. of Physics, Chung-Ang University, Seoul 06974, Republic of Korea
[65] Oskar Klein Centre and Dept. of Physics, Stockholm University, SE-10691 Stockholm, Sweden

[66] Dept. of Physics and Astronomy, Stony Brook University, Stony Brook, NY 11794-3800, USA
[67] Dept. of Physics, Sungkyunkwan University, Suwon 16419, Republic of Korea
[68] Institute of Physics, Academia Sinica, Taipei, 11529, Taiwan
[69] Earthquake Research Institute, University of Tokyo, Bunkyo, Tokyo 113-0032, Japan
[70] Dept. of Physics and Astronomy, University of Alabama, Tuscaloosa, AL 35487, USA
[71] Dept. of Astronomy and Astrophysics, Pennsylvania State University, University Park, PA 16802, USA
[72] Dept. of Physics, Pennsylvania State University, University Park, PA 16802, USA
[73] Institute of Gravitation and the Cosmos, Center for Multi-Messenger Astrophysics, Pennsylvania State University, University Park, PA 16802, USA
[74] Dept. of Physics and Astronomy, Uppsala University, Box 516, SE-75120 Uppsala, Sweden
[75] Dept. of Physics, University of Wuppertal, D-42119 Wuppertal, Germany
[76] Deutsches Elektronen-Synchrotron DESY, Platanenallee 6, D-15738 Zeuthen, Germany
[a] also at Institute of Physics, Sachivalaya Marg, Sainik School Post, Bhubaneswar 751005, India
[b] also at Department of Space, Earth and Environment, Chalmers University of Technology, 412 96 Gothenburg, Sweden
[c] also at INFN Padova, I-35131 Padova, Italy
[d] also at Earthquake Research Institute, University of Tokyo, Bunkyo, Tokyo 113-0032, Japan
[e] now at INFN Padova, I-35131 Padova, Italy

Acknowledgments

The authors gratefully acknowledge the support from the following agencies and institutions: USA – U.S. National Science Foundation-Office of Polar Programs, U.S. National Science Foundation-Physics Division, U.S. National Science Foundation-EPSCoR, U.S. National Science Foundation-Office of Advanced Cyberinfrastructure, Wisconsin Alumni Research Foundation, Center for High Throughput Computing (CHTC) at the University of Wisconsin–Madison, Open Science Grid (OSG), Partnership to Advance Throughput Computing (PATh), Advanced Cyberinfrastructure Coordination Ecosystem: Services & Support (ACCESS), Frontera and Ranch computing project at the Texas Advanced Computing Center, U.S. Department of Energy-National Energy Research Scientific Computing Center, Particle astrophysics research computing center at the University of Maryland, Institute for Cyber-Enabled Research at Michigan State University, Astroparticle physics computational facility at Marquette University, NVIDIA Corporation, and Google Cloud Platform; Belgium – Funds for Scientific Research (FRS-FNRS and FWO), FWO Odysseus and Big Science programmes, and Belgian Federal Science Policy Office (Belspo); Germany – Bundesministerium für Forschung, Technologie und Raumfahrt (BMFTR), Deutsche Forschungsgemeinschaft (DFG), Helmholtz Alliance for Astroparticle Physics (HAP), Initiative and Networking Fund of the Helmholtz Association, Deutsches Elektronen Synchrotron (DESY), and High Performance Computing cluster of the RWTH Aachen; Sweden – Swedish Research Council, Swedish Polar Research Secretariat, Swedish National Infrastructure for Computing (SNIC), and Knut and Alice Wallenberg Foundation; European Union – EGI Advanced Computing for research; Australia – Australian Research Council; Canada – Natural Sciences and Engineering Research Council of Canada, Calcul Québec, Compute Ontario, Canada Foundation for Innovation, WestGrid, and Digital Research Alliance of Canada; Denmark – Villum Fonden, Carlsberg Foundation, and European Commission; New Zealand – Marsden Fund; Japan – Japan Society for Promotion of Science (JSPS) and Institute for Global Prominent Research (IGPR) of Chiba University; Korea – National Research Foundation of Korea (NRF); Switzerland – Swiss National Science Foundation (SNSF).